

Herschel Planetary Nebula Survey (HerPlaNS)

First detection of OH⁺ in planetary nebulae^{*}

I. Aleman¹, T. Ueta^{2,3,**}, D. Ladjal², K. M. Exter⁴, J. H. Kastner⁵, R. Montez Jr.⁶, A. G. G. M. Tielens¹, Y.-H. Chu⁷,
H. Izumiura⁸, I. McDonald⁹, R. Sahai¹⁰, N. Siódmiak¹¹, R. Szczerba¹¹, P. A. M. van Hoof¹², E. Villaver¹³,
W. Vlemmings¹⁴, M. Wittkowski¹⁵, and A. A. Zijlstra⁹

¹ Leiden Observatory, University of Leiden, PO Box 9513, 2300 RA Leiden, The Netherlands

e-mail: aleman@strw.leidenuniv.nl

² Department of Physics and Astronomy, University of Denver, 2112 E. Wesley Ave., Denver, CO 80210, USA

³ Institute of Space and Astronautical Science, Japan Aerospace Exploration Agency, 3-1-1 Yoshinodai, Chuo-ku, Sagami-hara, 252-5210 Kanagawa, Japan

⁴ Instituut voor Sterrenkunde, Katholieke Universiteit Leuven, Celestijnenlaan 200D, 3001 Leuven, Belgium

⁵ Chester F. Carlson Center for Imaging Science and Laboratory for Multiwavelength Astrophysics, Rochester Institute of Technology, 54 Lomb Memorial Drive, Rochester, NY 14623, USA

⁶ Department of Physics and Astronomy, Vanderbilt University, Nashville, TN 37235, USA

⁷ Department of Astronomy, University of Illinois, 1002 W. Green St., Urbana, IL 61801, USA

⁸ Okayama Astrophysical Observatory, National Astronomical Observatory of Japan, 3037-5 Honjo, Kamogata, Asakuchi, 719-0232 Okayama, Japan

⁹ Jodrell Bank Centre for Astrophysics, Alan Turing Building, The University of Manchester, M13 9PL, UK

¹⁰ Jet Propulsion Laboratory, California Institute of Technology, Pasadena, CA 91109, USA

¹¹ N. Copernicus Astronomical Center, Rabianska 8, 87-100 Torun, Poland

¹² Royal Observatory of Belgium, Ringlaan 3, 1180 Brussel, Belgium

¹³ Universidad Autónoma de Madrid, Dpto. Física Teórica, Módulo 15, Facultad de Ciencias, Campus de Cantoblanco, 28049 Madrid, Spain

¹⁴ Department of Earth and Space Sciences, Chalmers University of Technology, Onsala Space Observatory, 439 92 Onsala, Sweden

¹⁵ ESO, Karl Schwarzschild Str. 2, 85748 Garching bei München, Germany

Received 29 October 2013 / Accepted 7 April 2014

ABSTRACT

Aims. We report the first detections of OH⁺ emission in planetary nebulae (PNe).

Methods. As part of an imaging and spectroscopy survey of 11 PNe in the far-IR using the PACS and SPIRE instruments aboard the *Herschel* Space Observatory, we performed a line survey in these PNe over the entire spectral range between 51 μm and 672 μm to look for new detections.

Results. The rotational emission lines of OH⁺ at 152.99, 290.20, 308.48, and 329.77 μm were detected in the spectra of three planetary nebulae: NGC 6445, NGC 6720, and NGC 6781. Excitation temperatures and column densities derived from these lines are in the range of 27–47 K and 2×10^{10} – 4×10^{11} cm⁻², respectively.

Conclusions. In PNe, the OH⁺ rotational line emission appears to be produced in the photodissociation region (PDR) in these objects. The emission of OH⁺ is observed only in PNe with hot central stars ($T_{\text{eff}} > 100\,000$ K), suggesting that high-energy photons may play a role in OH⁺ formation and its line excitation in these objects, as seems to be the case for ultraluminous galaxies.

Key words. astrochemistry – circumstellar matter – planetary nebulae: general – planetary nebulae: individual: NGC 6445 – planetary nebulae: individual: NGC 6720 – planetary nebulae: individual: NGC 6781

1. Introduction

The molecular ion OH⁺ plays an important role in the chemistry of oxygen-bearing species and in the formation of water in space (Herbst & Klemperer 1973; Barsuhn & Walmsley 1977; Sternberg & Dalgarno 1995; Hollenbach et al. 2012). Reactions of this molecular ion with H₂ can lead to the formation of H₂O⁺ and H₃O⁺, which recombine with electrons to form

water. Models indicate that the abundances of these species are sensitive to the flux of UV photons, X-rays, and cosmic rays (Meijerink et al. 2011; Hollenbach et al. 2012; Benz et al. 2013; González-Alfonso et al. 2013). Observations of OH⁺ and H₂O⁺ can be used, for example, to infer cosmic ray ionisation rates (Hollenbach et al. 2012). The OH⁺ molecular ion can also be produced in a medium ionised by shocks (Neufeld & Dalgarno 1989; de Almeida 1990; Kristensen et al. 2013, and references therein).

In the interstellar medium (ISM), OH⁺ is thought to be formed through two main routes (see Sternberg & Dalgarno 1995; Meijerink et al. 2011; Hollenbach et al. 2012): one is the

* *Herschel* is an ESA space observatory with science instruments provided by European-led Principal Investigator consortia and with important participation from NASA.

** JSPS FY2013 Long-Term Invitation Fellow.

Table 1. Data^a for PNe surveyed for OH⁺.

PN	T_* (10^3 K)	Distance (kpc)	Radius (pc)	H ₂	X-Rays ^b	C/O ^c	Morphology ^d
Detections							
NGC 6445	170	1.39	0.14	Y	P	0.45	Mpi
NGC 6720	148	0.70	0.13	Y	N	0.62	Ecsh
NGC 6853 ^e	135	0.38	0.37	Y	P	–	Bbpih
NGC 6781	112	0.95	0.32	Y	N	1.0–1.5	Bth
NGC 7293 ^e	110	0.22	0.46	Y	P	0.87	Ltspir
Non-detections							
NGC 7027 ^e	175	0.89	0.03	Y	D	2.29	Mctspih
Mz 3	107 ^f	1.30	0.1–0.2	N ^g	D, P	0.83	Bps
NGC 3242	89	0.81	0.13	N	D	–	Ecspaih
NGC 7009	87	1.45	0.09	N	D, P	0.32	Lbspa
NGC 7026	83 ^f	1.70	0.16	Y ^h	D, P?	–	Mcbps
NGC 6826	50	1.30	0.08	N	D, P	0.87	Ecsah
NGC 40	48	1.02	0.11	Y ^h	D	1.41	Bbsh
NGC 6543	48	1.50	0.09	N	D, P	0.44	Mcspa
NGC 2392	47	1.28	0.14	N	D, P	1.14	Rsai

Notes. ^(a) Most of the data in the table are from [Kastner et al. \(2012\)](#) and [Ueta et al. \(2014\)](#), exceptions are noted; ^(b) N = non-detection, P = point-like source, D = diffuse emission; ^(c) carbon to oxygen ratios from [Henry et al. \(1999\)](#), [Cohen & Barlow \(2005\)](#), [Pottasch & Bernard-Salas \(2010\)](#), and [Ueta et al. \(2014\)](#); ^(d) according to the classification scheme by [Sahai et al. \(2011\)](#); ^(e) Not a HerPlaNS target, see [Wesson et al. \(2010\)](#) and [Etxaluze et al. \(2014\)](#); ^(f) [Phillips \(2003\)](#); ^(g) [Smith \(2003\)](#); ^(h) [Hora et al. \(1999\)](#).

reaction of O⁺ with H₂ and the other the reaction of O with H₃⁺. As shown by [Hollenbach et al. \(2012\)](#), the former route will produce OH⁺ more efficiently close to $A_V \sim 0.1$ and the latter around $A_V \sim 6$ (where the precise value depends on the intensity of the radiation field).

In photodissociation regions (PDRs), in addition to the reaction between O⁺ and H₂, photoionisation of OH and charge exchange between OH and H⁺ may also contribute to OH⁺ formation ([Meijerink et al. 2011](#); [van der Tak et al. 2013](#)). Furthermore, PDR models ([Hollenbach et al. 2012](#)) show that the production of OH⁺ is more efficient in two different regimes: (i) low-density clouds with low levels of ultraviolet (UV) radiation ($\chi \sim 1\text{--}10^3$ and $n < 10^3 \text{ cm}^{-3}$) and (ii) high-density environments with high levels of UV radiation ($\chi \sim 10^4\text{--}10^5$ and $n > 10^5 \text{ cm}^{-3}$), where χ is defined as the ratio between the fluxes of the source and of the interstellar radiation field at $h\nu = 12.4 \text{ eV}$ ($=1000 \text{ \AA}$) and hence is a measure of the radiation field strength (e.g. [Draine & Bertoldi 1996](#)).

In most sources where OH⁺ has been detected, its lines are seen in absorption and are usually attributed to diffuse interstellar clouds ionised by the galactic interstellar radiation field and cosmic rays, or by far-ultraviolet photons from nearby stars. The first detection of OH⁺ in the ISM was made by [Wyrowski et al. \(2010\)](#) towards the giant molecular cloud Sagittarius B2 using the Atacama Pathfinder Experiment (APEX) telescope. Absorption lines of OH⁺ have also been detected along several lines of sight in the Galactic ISM towards bright continuum sources, such as the Orion molecular clouds ([Gerin et al. 2010](#); [Neufeld et al. 2010](#); [Gupta et al. 2010](#); [Indriolo et al. 2012](#); [López-Sepulcre et al. 2013](#)) and the massive star-forming region W3 IRS5 ([Benz et al. 2013](#)). Lines of OH⁺ have also been detected in absorption in the material around young stars ([van Dishoeck et al. 2011](#); [Benz et al. 2013](#); [Kristensen et al. 2013](#); [Kama et al. 2013](#)) and in the galaxies NGC 4418 and Arp 220 ([Rangwala et al. 2011](#); [González-Alfonso et al. 2013](#)).

Emission lines of OH⁺ have been observed in ultraluminous galaxies, e.g. Mrk 231 ([van der Werf et al. 2010](#)) and NGC 7130 ([Pereira-Santaella et al. 2013](#)). In Mrk 231, for example, the

detected lines correspond to transitions between the first excited and the ground rotational levels. The powerful OH⁺ emission in such objects is attributed to the chemistry in X-ray dominated regions (XDRs; [van der Werf et al. 2010](#)).

In our Galaxy, detection of OH⁺ lines in emission has so far been limited to the Orion bar, the prototypical PDR, where [van der Tak et al. \(2013\)](#) has reported the detection of the lines at 290.20, 308.48, and 329.77 μm (the transitions from $N = 1$ to $N = 0$), and to the Crab nebula supernova remnant, where [Barlow et al. \(2013\)](#) detected the line at 308.48 μm . In [van der Tak et al. \(2013\)](#), the presence of OH⁺ is analysed in terms of PDR models, with the conclusion that the emission from OH⁺ is largely due to the PDR produced by the nearby Trapezium stars ($\chi \sim 10^4\text{--}10^5$ and $n \geq 10^5 \text{ cm}^{-3}$).

We report the first detections of OH⁺ in planetary nebulae (PNe), the ejecta of evolved low- to intermediate-mass stars. This discovery was made simultaneously, but independently with the detection of OH⁺ in NGC 7293 and NGC 6853 by [Etxaluze et al. \(2014\)](#), also published in this volume.

2. Observations

The *Herschel* Planetary Nebula Survey (HerPlaNS; [Ueta et al. 2014](#)) obtained far-infrared broadband images and spectra of eleven well-known PNe with the PACS ([Poglitsch et al. 2010](#)) and SPIRE ([Griffin et al. 2010](#)) instruments onboard the *Herschel* Space Observatory ([Pilbratt et al. 2010](#)). The target list is volume-limited – all the PNe have distances $\leq 1.5 \text{ kpc}$ – and is dominated by relatively high-excitation nebulae. The HerPlaNS PNe were selected from the initial *Chandra* Planetary Nebula Survey (ChanPlaNS; [Kastner et al. 2012](#)) target list and take into account the far-IR detectability of the target candidates, which was based on previous observations made with IRAS, ISO, *Spitzer*, and AKARI. One of the objectives of this selection is to investigate potential effects of X-rays on the physics and chemistry of the nebular gas and their manifestations in far-IR emission. The PNe in the sample are listed in Table 1 together with some of their properties. The objects NGC 7293, NGC 6853,

and NGC 7027 (Wesson et al. 2010; Etxaluze et al. 2014), which have also been observed with *Herschel*, are included for comparison. Below, we provide a short description of the observations and data reduction techniques. A more detailed description is provided in Ueta et al. (2014).

In this paper, we make use of far-IR spectroscopic data acquired by HerPlaNS. These data consist of 25 integral-field-unit (IFU) spectra in the PACS band, 35 Fourier-transform spectrometer (FTS) spectra in the SPIRE SSW band, and 19 FTS spectra in the SPIRE SLW band at multiple locations around the target PN (hereafter pointings). With PACS, we performed spectroscopy in two overlapping bands to cover 51–220 μm with a velocity resolution of $\sim 75\text{--}300 \text{ km s}^{-1}$ over a $47'' \times 47''$ field of view covered by 5×5 spaxels (i.e. spectral pixels). With SPIRE, we performed spectroscopy in two overlapping bands to cover 194–672 μm (SSW band 194–313 μm with 35 detectors and SLW band 303–672 μm with 19 detectors).

Data reduction for PACS observations was performed with HIPE version 11, calibration release version 44, using the background normalisation PACS spectroscopy pipeline script. We followed the reduction steps described in the PACS Data Reduction Guide: Spectroscopy¹. For SPIRE data reduction we used HIPE version 11 with calibration tree version 11. We followed the standard HIPE-SPIRE spectroscopy data reduction pipeline for the single-pointing mode described in the SPIRE Data Reduction Guide² with the following modifications: instead of treating only the signal from the central of signal only from the central bolometer, as nominally done for processing the single-pointing observations, the signal from each bolometer was individually extracted and reduced; extended source flux calibration correction was applied; and background subtraction was made using our own dedicated off-target sky observations.

The top panels in Figs. 1–3 show the footprints of the PACS spaxels (each square indicates a spaxel) and of the SPIRE central bolometers (circles) for the three HerPlaNS PNe that are the focus of this paper: NGC 6781, NGC 6720, and NGC 6445, respectively. For NGC 6781, spectra were obtained at two different PACS pointings, one towards the centre and the other towards the west rim, while for NGC 6720 and NGC 6445, spectra were taken at one pointing for each PN. For each of the three PNe, SPIRE spectra were acquired at two different pointings: one towards the centre and the other towards a bright feature (the west rim for NGC 6781, the north rim for NGC 6720, and the north lobe for NGC 6445).

3. The Detection of OH⁺ Lines

In three of the eleven PNe observed in HerPlaNS – namely NGC 6445, NGC 6720, and NGC 6781 – we identified four lines of OH⁺ in emission: the line at 152.99 μm in the PACS spectra and the lines at 290.20, 308.48, and 329.77 μm in the SPIRE spectra. These lines are produced by the lowest rotational transitions of the OH⁺ electronic ground state, as can be seen in the OH⁺ levels diagram in Fig. 4. In this figure, the detected transitions are indicated as solid red vertical lines. The dashed line indicates the transition that produces the line at 152.37 μm , which is detected (with signal-to-noise ratio above 3.0) only in the PACS spectra of NGC 6445. In addition, we also identified two

¹ http://herschel.esac.esa.int/hcss-doc-9.0/load/pacs_spec/html/pacs_spec.html (Version 1, Aug. 2012).

² http://herschel.esac.esa.int/hcss-doc-9.0/load/spire_drg/html/spire_drg.html (version 2.1, Document Number: SPIRE-RAL-DOC 003248, 06 July 2012).

Table 2. OH⁺ and OH lines detected with PACS.

	λ_0 (μm)	λ_{OBS} (μm)	Surface brightness ^a	S/N^b
NGC 6781 – centre				
OH	119.23	119.24	(4.1 ± 0.7)	2.4
OH	119.44	119.43	(4.5 ± 0.8)	2.1
OH ⁺	152.99	153.02	2.2 ± 0.5	4.9
NGC 6781 – west rim				
OH	119.23	119.25	12.4 ± 2.8	5.1
OH	119.44	119.44	12.9 ± 2.3	6.8
OH ⁺	152.99	153.03	3.6 ± 0.6	5.6
NGC 6720				
OH	119.23	119.26	11.6 ± 1.4	9.1
OH	119.44	119.44	11.4 ± 1.6	7.5
OH ⁺	152.99	153.02	3.2 ± 0.9	7.5
NGC 6445				
OH	119.23	119.24	0.245 ± 0.020	8.1
OH	119.44	119.44	0.24 ± 0.04	12
OH ⁺	152.37	152.42	2.6 ± 0.7	3.7
OH ⁺	152.99	153.01	3.7 ± 0.8	6.7

Notes. ^(a) Surface brightness in $10^{-17} \text{ erg cm}^{-2} \text{ s}^{-1} \text{ arcsec}^{-2}$. See text for details on the measurements. Numbers in parentheses are below the 3σ detection limit. Errors obtained from the reduction process are shown. The absolute calibration uncertainty is 30% and should be added to these values. ^(b) Signal-to-noise ratio.

spectral lines at 119.23 μm and 119.44 μm as the OH ${}^2\Pi_{3/2}J = 5/2\text{--}3/2$ doublet produced by the transitions between the lowest rotational levels of OH. For line identification, we use the wavelengths provided by the Cologne Database for Molecular Spectroscopy³ (Müller et al. 2005) and the Jet Propulsion Laboratory Molecular Spectroscopy Catalogue⁴ (Pickett et al. 1998).

The spectra around the detected OH⁺ and OH lines are shown in Figs. 5 and 6 for the three PNe mentioned above. For PACS spectra (Fig. 5), the plots display the spectra obtained by summing the flux of spectra extracted from all individual spaxels and dividing by the total aperture ($47'' \times 47''$). It is important to note that by simply summing the spaxel fluxes, we are ignoring effects such as the point spread function (PSF) width exceeding the spaxel size. In the case of NGC 6781, we provide the spectra for the two pointings. The surface brightnesses of the OH⁺ and OH lines detected with PACS are listed in Table 2.

For SPIRE observations (Fig. 6), the plots show the spectra obtained with the central bolometer for the two pointings for each PNe. The surface brightnesses of the OH⁺ lines detected with SPIRE are given in Table 3. No corrections for the wavelength dependence of the SPIRE bolometer beam size were made.

In addition to the OH and OH⁺ lines, the PACS and SPIRE spectra of the three PNe detected in OH⁺ also show intense atomic and ionic forbidden lines and CO rotational lines (Ueta et al. 2014). There is no evidence of other species that could be responsible for the features we attribute here to OH⁺.

³ Spectroscopic parameters of OH⁺ published in the *Cologne Database for Molecular Spectroscopy* (<http://www.astro.uni-koeln.de/cdms>) and used here were based on data obtained by Bekooy et al. (1985) and Werner et al. (1983).

⁴ Spectroscopic parameters of OH published in the *Jet Propulsion Laboratory Molecular Spectroscopy Catalogue* (<http://spec.jpl.nasa.gov>) were based on data obtained by Drouin (2013), Peterson et al. (1984), and references therein.

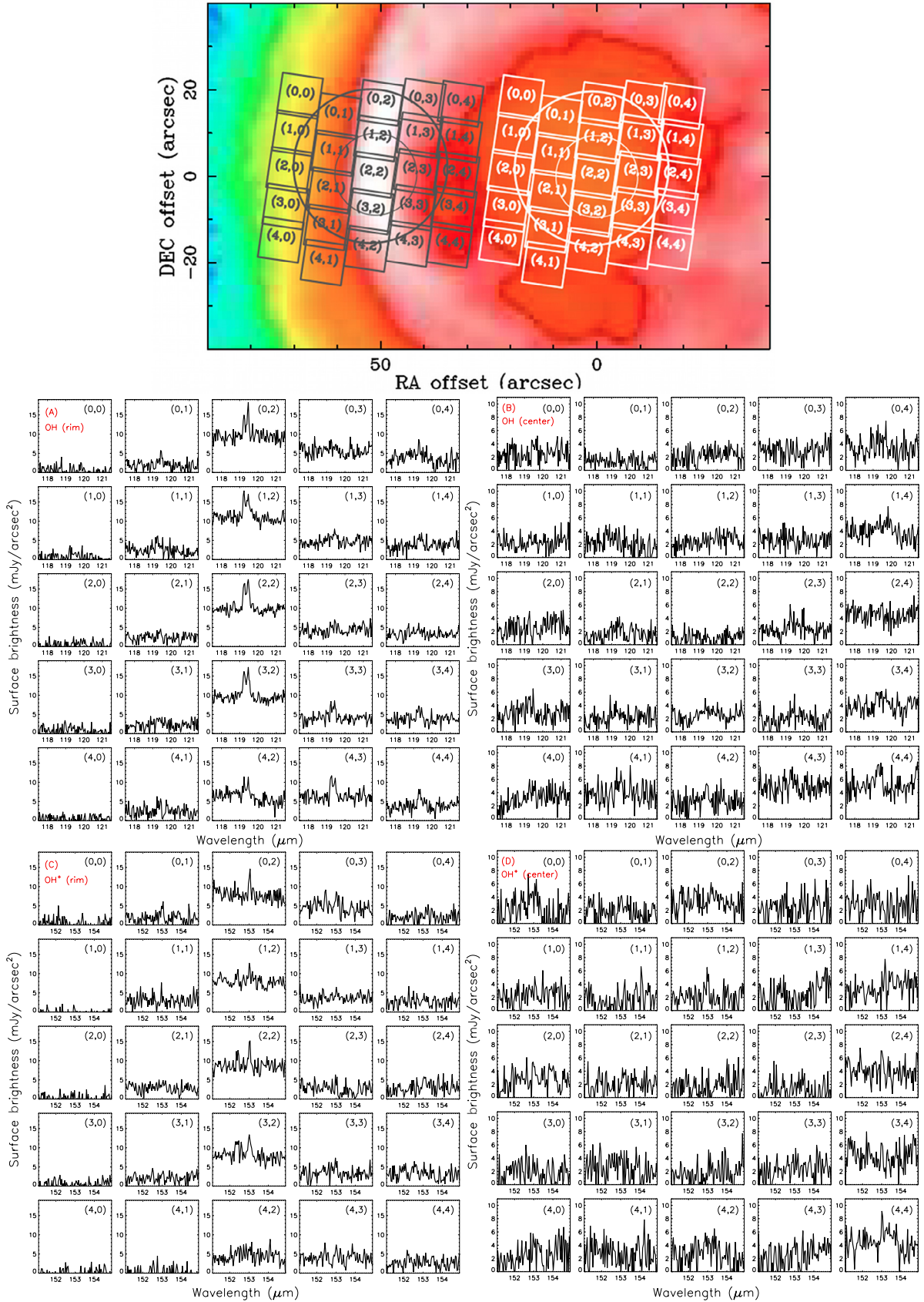


Fig. 1. Measurements of lines of OH and OH⁺ in the HerPlaNS observations of NGC 6781. The *top panel* shows the locations of individual PACS spaxels (boxes) and of the central SPIRE SSW and SLW bolometers (circles) for the rim (grey) and centre (white) pointing. In the figure, north is up and the celestial coordinates of the point (0,0) are $(\alpha, \delta) = (19:18:28.089, 6:32:19.262)$. The footprints are shown over the PACS 70 μm image. Labels indicate specific spaxels. Panels **A**) and **B**) show the spatial variation of the OH 119.3 μm doublet and panels **C**) and **D**) show the OH⁺ 152.99 μm line emission in NGC 6781 (rim pointing on the left; centre pointing on the right). Individual PACS spaxels are indicated by the numbers in parentheses. Dust emission is responsible for the differences in the continuum levels.

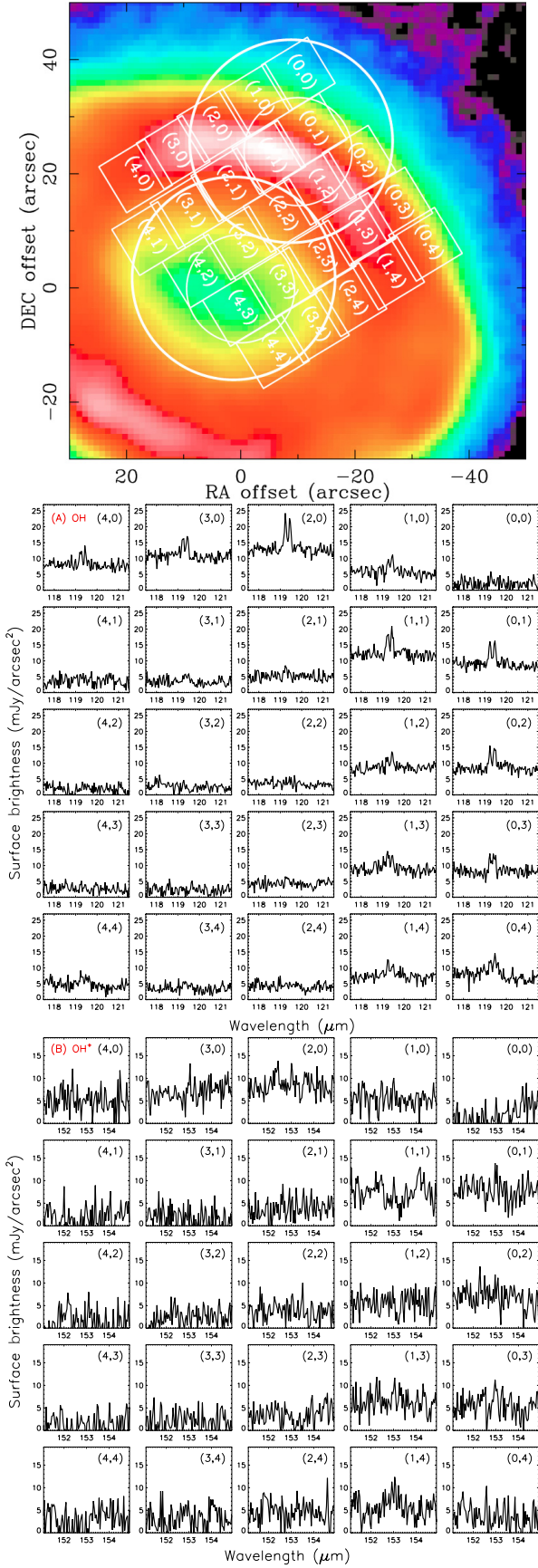


Fig. 2. Same as Fig. 1, but for NGC 6720. In the *top panel*, north is up and the celestial coordinates of the point (0, 0) are $(\alpha, \delta) = (18:53:35.080, 33:01:44.869)$. The order of the spaxels in plots **A**) and **B**) is different from Fig. 1; the order was chosen to be more convenient for comparison to the footprints in the *top image of this figure*.

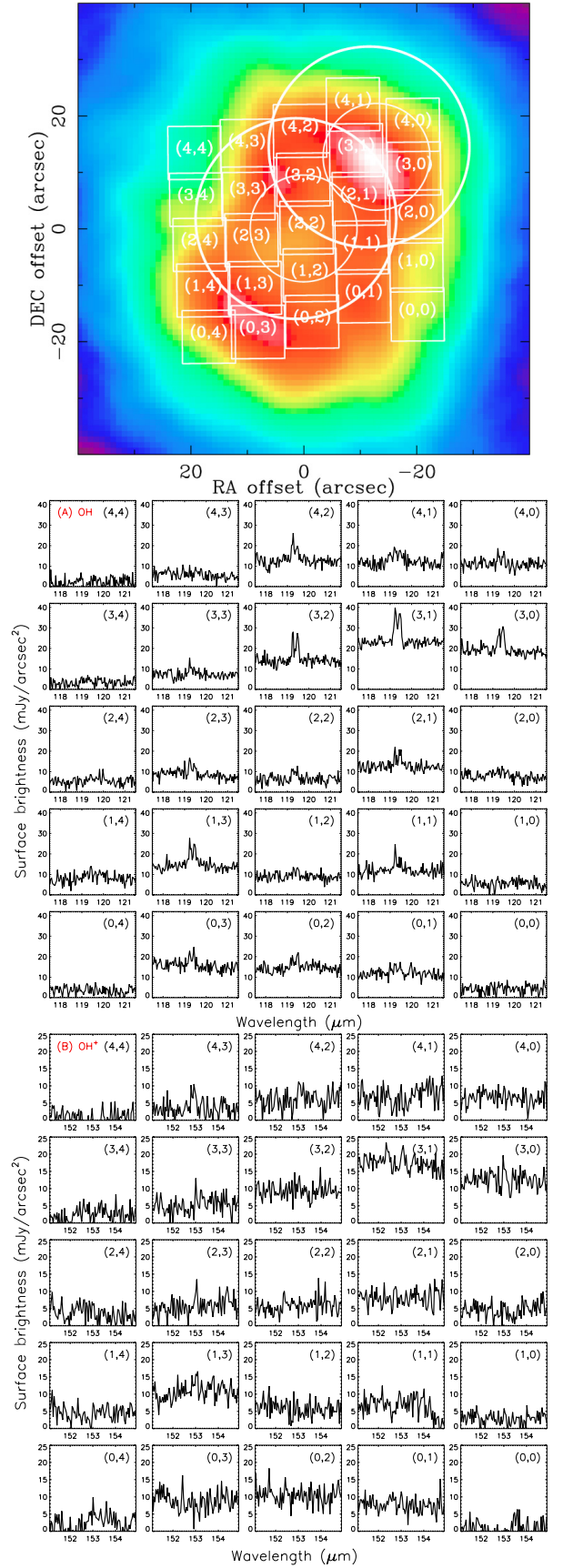


Fig. 3. Same as Fig. 1, but for NGC 6445. In the *top panel*, north is up and the celestial coordinates of the point (0, 0) are $(\alpha, \delta) = (17:49:15.215, -20:00:34.427)$. The order of the spaxels in plots **A**) and **B**) is different from Fig. 1; the order was chosen to be more convenient for comparison to the footprints in the *top image of this figure*.

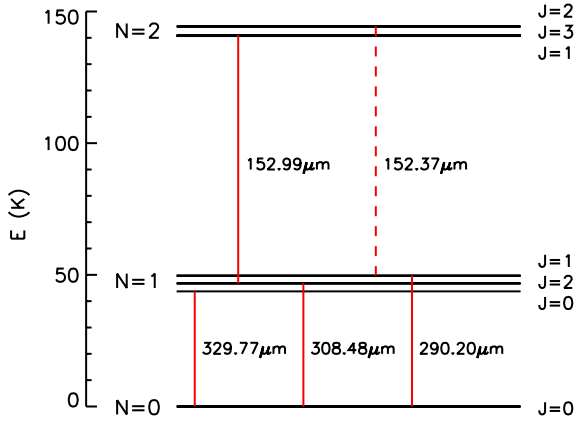


Fig. 4. The three lowest rotational energy levels of OH⁺. Except for the $N = 0$ level, each rotational level is split into three fine structure levels. The energy difference between levels $J = 1$ and $J = 3$ of $N = 2$ is not resolved in the figure. The hyperfine structure, which further splits the levels, is not indicated in the figure. The transitions corresponding to the lines detected in the present work are indicated in red (with the corresponding wavelength); the dashed line represents a line detected only in NGC 6445.

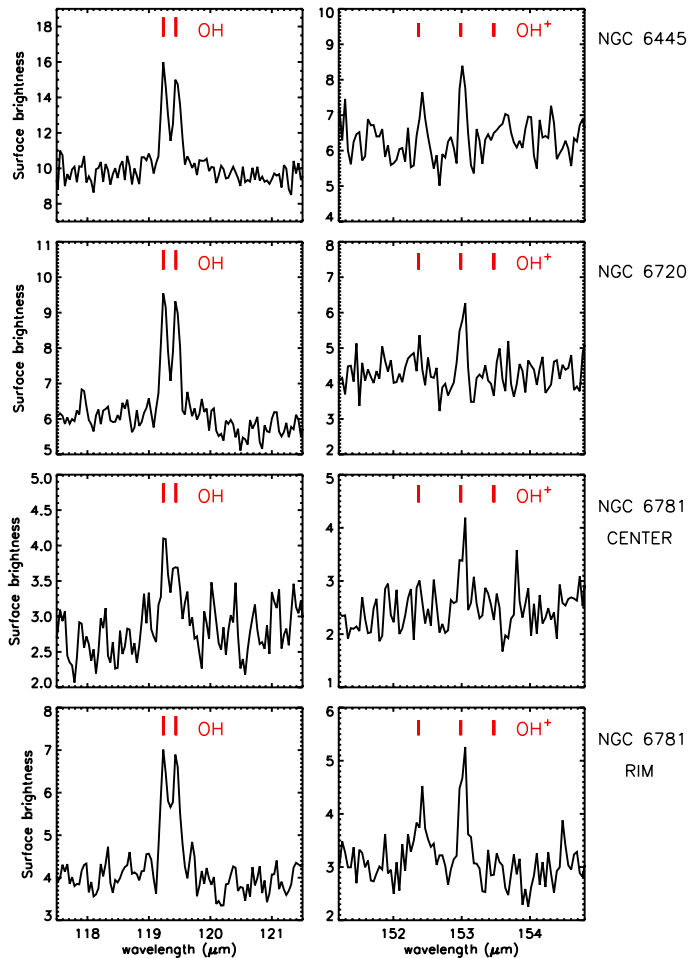


Fig. 5. Lines of OH and OH⁺ detected in the PACS spectra of NGC 6445, NGC 6720, and NGC 6781 (in this case, for both the centre and rim pointings) obtained in the HerPlaNS program. The left panels show the OH doublet, while the panels on the right show the OH⁺ lines. The expected positions of the lines are indicated in each plot. The spectra are obtained by integrating the flux of spectra extracted from all individual spaxels and dividing by the total aperture. The surface brightness is given in Jy/arcsec². See details of the pointings in Figs. 1–3.

Table 3. OH⁺ lines detected with SPIRE.

	λ_0 (μm)	λ_{OBS} (μm)	Surface brightness ^a	S/N^b
NGC 6781 – centre				
OH ⁺	290.20	290.20	$(2.2 \pm 1.0)^b$	2.7
OH ⁺	308.48	308.77	1.10 ± 0.09	12
OH ⁺	329.77	329.95	0.24 ± 0.12	5.8
NGC 6781 – west rim				
OH ⁺	290.20	290.37	6.0 ± 0.9	9.2
OH ⁺	308.48	308.65	0.99 ± 0.03	30
OH ⁺	329.77	329.90	0.11 ± 0.10	6.4
NGC 6720 – centre				
OH ⁺	290.20	290.05	1.68 ± 0.20	6.9
OH ⁺	308.48	308.45	2.18 ± 0.07	27
OH ⁺	329.77	329.52	0.40 ± 0.06	5.9
NGC 6720 – north rim				
OH ⁺	290.20	290.14	3.7 ± 0.4	9.3
OH ⁺	308.48	308.39	3.74 ± 0.11	28
OH ⁺	329.77	329.76	1.00 ± 0.09	8.5
NGC 6445 – centre				
OH ⁺	290.20	290.12	(0.93 ± 0.13)	2.7
OH ⁺	308.48	308.47	2.64 ± 0.09	24
OH ⁺	329.77	329.64	0.91 ± 0.10	6.7
NGC 6445 – lobe				
OH ⁺	290.20	290.21	1.56 ± 0.13	11
OH ⁺	308.48	308.49	2.40 ± 0.10	20
OH ⁺	329.77	329.78	0.43 ± 0.04	10

Notes. ^(a) Surface brightness in 10^{-17} erg cm⁻² s⁻¹ arcsec⁻². See text for details on the measurements. Numbers in parentheses are below the 3σ detection limit. Errors obtained from the reduction process are shown. ^(b) Signal-to-noise ratio.

Figure 1 shows the spatial variation of the OH lines at $119.23 \mu\text{m}$ and $119.44 \mu\text{m}$ and the OH⁺ line at $152.99 \mu\text{m}$ for NGC 6781. The emission of these lines comes mostly from the dusty ring structure. In the east rim pointing, for example, the emission correlates well with the dust emission peaks. This is also the case for NGC 6720 and NGC 6445 (Figs. 2 and 3), where the OH⁺ emission peaks at the north rim and the (north-west and south-east) lobes, respectively. For these two PNe, OH⁺ emission from individual spaxels is faint and it is necessary to integrate the emission over a few spaxels to obtain a signal-to-noise ratio >3 . The northwest and southeast lobes of NGC 6445 and the rims in NGC 6720 and NGC 6781 correspond to bright regions in the waist of these multi/bipolar PNe (Zuckerman et al. 1990; Benítez et al. 2005; O’Dell et al. 2013). These structures also display bright H₂ emission at $2.12 \mu\text{m}$ and [NII] $\lambda 6584$ line emission (Zuckerman et al. 1990; Kastner et al. 1996; O’Dell et al. 2013).

4. Discussion

As shown above, most of the OH⁺ line emission comes from the pointings towards the ring-like or torus-like structures (where the column density is high), at the interface between the ionised region and the PDR in the PNe we studied. It is natural then to expect that the strong radiation field from the central star in this region plays a major role in the chemistry. PDR models show that the column density of OH⁺ is enhanced in dense and high UV field environments (Hollenbach et al. 2012), e.g. for conditions like those in the Orion bar ($n \geq 10^5$ cm⁻³ and $\chi \sim 10^4$ – 10^5 ; van der Tak et al. 2013).

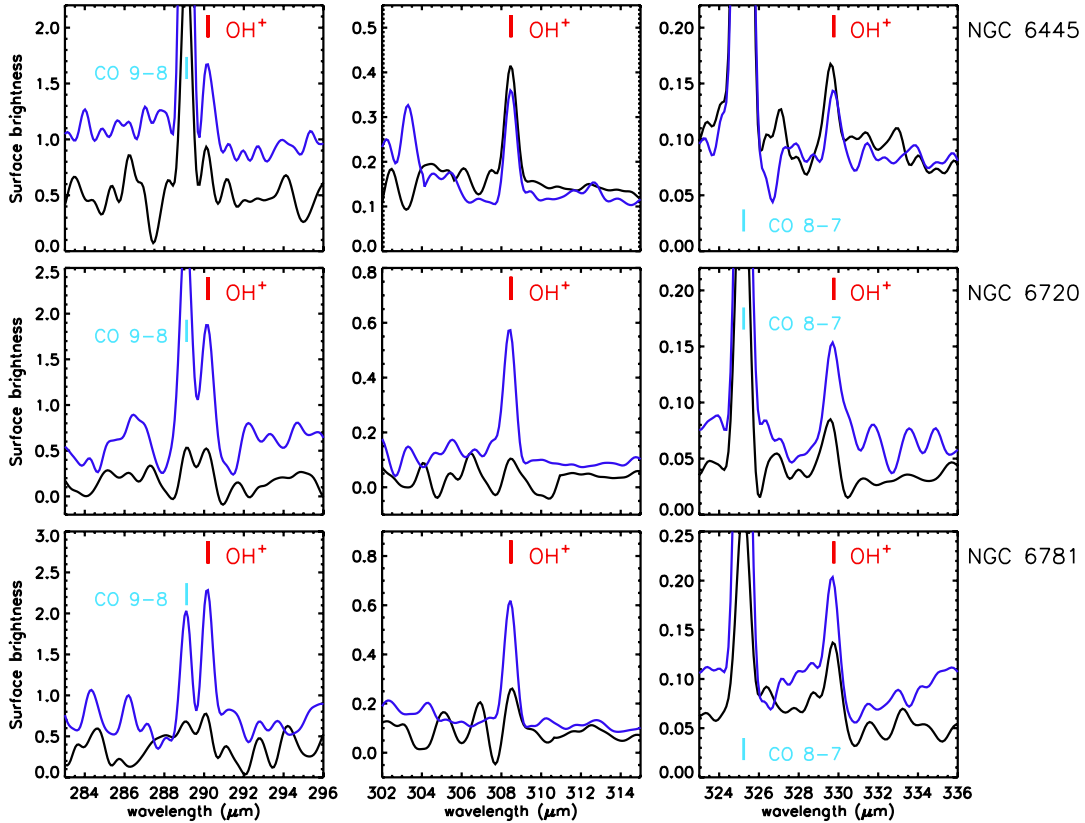


Fig. 6. Lines of OH^+ detected in the SPIRE spectra of NGC 6445, NGC 6720, and NGC 6781 obtained in the HerPlaNS programme. The expected positions of the lines are indicated in each plot. The plots show the spectra obtained with the central bolometer; the spectra in black correspond to the pointing towards the centre of each PN, while the blue is centred in the north lobe of NGC 6445, the north rim of NGC 6720, and the west rim of NGC 6781. The surface brightness is given in Jy/arcsec^2 . See details of the pointings in Figs. 1–3.

From this we suggest that the five PNe with OH^+ (here we include NGC 7293 and NGC 6853; see [Etxaluze et al. 2014](#)) may contain PDRs with densities similar to the Orion bar. These PDRs could be associated with the cometary knots, dense clumps embedded in the diffuse ionised gas of PNe. Observations show that all the PNe detected in OH^+ have cometary knots ([Kastner et al. 1996](#); [O’Dell et al. 2002](#); [Phillips et al. 2011](#)). The diffuse ionised gas in PNe has typical densities of 10^2 – 10^4 cm^{-3} , while the PNe cometary knots have densities similar to the Orion bar ($>10^5 \text{ cm}^{-3}$). Considering that we detect OH^+ in the same region where cometary knots are identified in optical images, and in this region we have strong UV fields, it is likely that the OH^+ emission should be associated with the cometary knots.

A simple calculation using the values in Table 1 and assuming the luminosity values of $L = 385$, 200, and $1035 L_{\odot}$ for the central stars of NGC 6781, NGC 6720, and NGC 6445, respectively, allows us to estimate χ in the PDRs for these PNe. For this calculation, we also assume that (i) the central star emits as a blackbody; (ii) there is no radiation extinction within the nebula; (iii) there is no contribution from the secondary photons; and (iv) the distance of the PDR from the central star is equal to the distance from the centre of the PN to the structure that emits OH^+ projected on the sky. We obtain $\chi = 3.2$, 5.0, and 16, respectively. Given these assumptions, the PDR density can be estimated from the ionised gas density assuming pressure equilibrium at a typical temperature contrast of a factor of 20 ($T_{\text{ionised gas}} \sim 10000 \text{ K}$ vs. $T_{\text{PDR}} \sim 500 \text{ K}$; [Tielens 2005](#), Sect. 9.1). For NGC 6781, for example, $n_{\text{ionised gas}} = 600 \text{ cm}^{-3}$

([Ueta et al. 2014](#)) assuming $n_{\text{PDR}} = 12000 \text{ cm}^{-3}$. Thus, in terms of density, the PDRs in these PNe are comparable to the Orion bar, while the UV fields (6–13.6 eV) incident in these PDRs are much less than in the Orion bar.

All five PNe with OH^+ emission are detected in H_2 (Table 1) and CO ([Phillips et al. 1992](#); [Huggins et al. 1996](#); [Zack & Ziurys 2013](#)). Other molecules have been previously detected in NGC 6720, NGC 6781, and NGC 7293 (HCO^+ , HCN, HNC, and CN; [Bachiller et al. 1997](#); [Hasegawa 2003](#)). In the HerPlaNS PNe spectra, in addition to OH^+ and OH and intense atomic lines, there are clear lines of CO (the panels in the first column in Fig. 6 show the CO $J = 9-8$ line, for example) and possibly CH^+ .

The density of OH^+ can be enhanced in X-ray dominated regions, as in active galactic nuclei ([van der Werf et al. 2010](#)). In XDRs ([Meijerink & Spaans 2005](#)), photons with $E > 1 \text{ keV}$, which can penetrate high column density gas, can enhance the gas ionisation fraction and increase the gas temperature in the neutral or molecular region. In a similar fashion, soft X-rays ($E < 200 \text{ eV}$) can produce an extended warm semi-ionised region in the transition zone between the ionised region and the PDR. The enhanced ionisation fraction and warm gas temperature in these regions influences the ongoing chemistry and also the excitation of molecular emission lines in PNe (e.g. [Aleman & Gruenwald 2011](#); [Kimura et al. 2012](#)).

The central stars of all PNe detected in OH^+ have high effective temperatures (for all of them T_{eff} exceeds 100000 K ; Table 1) and produce soft X-ray emission. For PNe central stars, the flux of photons with energies greater than 100 eV increases

steeply with T_{eff} , reaching its maximum for $T_{\text{eff}} > 100\,000$ K (see Fig. 4 of Phillips 2006). Three out of five PNe thus far detected in OH^+ emission show X-ray emission in the form of *Chandra* detections of point-like emission at their central stars (Table 1; Kastner et al. 2012; Guerrero et al. 2001). One of these PN X-ray sources, NGC 6853, is very soft (all detected X-ray photons have energies <300 eV) and likely represents the Wien tail of a hot central star photosphere; the second, NGC 6445, is a relatively hard X-ray source, peaking near ~ 1 keV; and the third, NGC 7293, resembles a hybrid of these two X-ray source types. The non-detections of soft (<1 keV) X-rays from the hot central stars of NGC 6720 and NGC 6781, and the lack of an NGC 6853-like soft component in NGC 6445, is understandable if one notes that (a) these three molecule-rich PNe are significantly more distant than NGC 6853 and NGC 7923; and (b) all three lie along the Galactic plane, where the hydrogen column density is high. In fact, the *Chandra* results do not rule out the possibility that the central star of NGC 6781 could have a 1 keV X-ray flux similar to that of the central star of NGC 7293.

However, it appears significant that OH^+ has now been detected in both NGC 6853, the soft X-ray source, and NGC 7293, the soft/hard hybrid source. These detections – and the non-detection of OH^+ from molecule-rich NGC 7027 (see below), which harbours a significant (albeit diffuse) source of ~ 1 keV X-ray emission due to large-scale shocks (Kastner et al. 2012) – might indicate that it is the soft X-rays (<300 eV) of the central star, rather than relatively hard (~ 1 keV) X-rays, that drive OH^+ production in PNe.

Two other PNe with high-temperature central stars, NGC 7027 (Wesson et al. 2010) and Mz 3, do not show OH^+ . Hence, other factors, such as the density or carbon-to-oxygen ratio, may also play a role. Models of XDRs show that high column densities of OH^+ require not only high X-ray fluxes, but also high densities (Meijerink et al. 2011). The planetary nebula NGC 7027 is the prototypical PN with a PDR. The absence of OH^+ could be linked to the carbon-rich chemistry in this nebula (i.e. a significant fraction of the oxygen in the molecular region is in the form of CO), but NGC 6781 is also carbon-rich (Ueta et al. 2014). Etxaluze et al. (2014) show that other oxygen-bearing molecules could be formed in carbon-rich gas when the strong radiation field keeps CO partially dissociated in the PDR. Further modelling, now compared with data from the PNe where OH^+ is detected, would help clarify this question.

We note that none of our objects shows OH maser emission, which is common in young PNe with dense shells (Zijlstra et al. 2001). Either the density of OH decreases (e.g. by photoionisation) or the velocity coherence is lost in the evolution.

The OH^+ excitation diagrams for our three objects are shown in Fig. 7. The PACS and SPIRE instruments have different apertures. Moreover, SPIRE has a wavelength dependent aperture. To compare the lines from these different instruments in Fig. 7, we did the following calculations. For PACS, we average the surface brightness of the spaxels spatially coincident with the SPIRE central bolometer aperture at $290.20\ \mu\text{m}$. For the SPIRE lines, we assume that the surface brightness was uniformly distributed over the beam. Judging from the dust emission maps, we expect the PDR maps to fill at least half of the SPIRE beam. This assumption would only marginally affect the derived column densities and excitation temperatures. Using the values from Fig. 7, we derive OH^+ excitation temperatures between 27 K and 47 K and column densities between $2 \times 10^{10}\ \text{cm}^{-2}$ and $4 \times 10^{11}\ \text{cm}^{-2}$. For these calculations, we assume that the emission is optically thin.

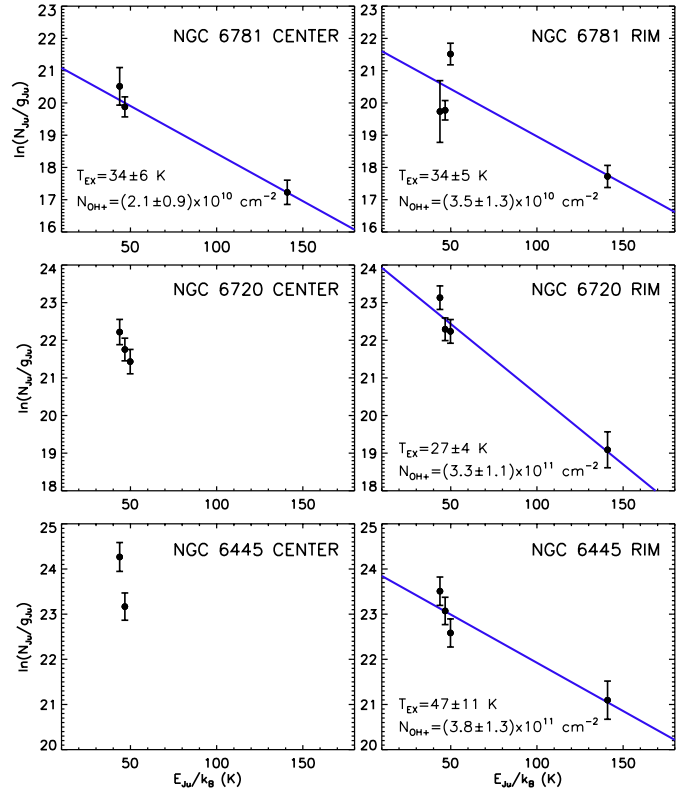


Fig. 7. Excitation diagrams for OH^+ . Dots are values obtained from our observations. Column densities are given in cm^{-2} . The solid lines are least-square fits to the data. The derived excitation temperatures and column densities are shown in corresponding panels. Fits are not provided when the calculated inclination coefficient is negative or when the uncertainty in the excitation temperature is greater than 50%.

Extensive excitation calculations have been performed by van der Tak et al. (2013) for the Orion bar PDR. That study shows that the excitation of the OH^+ levels is due to a combination of excitation by radiation, collisions, and formation pumping. Hence, the observed low excitation temperature for these OH^+ lines in the Orion bar (~ 9 K) is not a real kinetic temperature.

If we consider only lines in the SPIRE wavelength range, we also derive low excitation temperatures for these low lying levels (3–7 K). As for the Orion bar, we expect that this is not a real kinetic temperature. The additional OH^+ line that we observed with PACS would indicate a higher excitation temperature. If we include the line at $153\ \mu\text{m}$ (detected with PACS), we measure a much higher excitation temperature – directly reflecting the higher energy needed to excite this last line – than the excitation temperature derived using only SPIRE lines. Hence, we have elected to derive column densities including all the transitions (solid lines in Fig. 7). This is an approximate calculation, since we assume an LTE approximation, and clearly from Fig. 7 this is not the case. Our column densities are approximately 10 times lower than the column density of van der Tak et al. (2013) for the Orion bar, but the van der Tak et al. study lacked the higher excitation PACS line.

Using the values of χ and the column densities we derive above in Eq. (2) in Hollenbach et al. (2012), we estimate that the densities of the PDRs in NGC 6781, NGC 6720, and NGC 6445 lie within the range 10^3 – $10^4\ \text{cm}^{-3}$.

5. Conclusions

We present here the first detections of OH⁺ in PNe. The emission was detected in both PACS and SPIRE far-infrared spectra of three of the 11 PNe in the sample obtained in the *Herschel* Planetary Nebulae Survey (HerPlaNS). The simultaneous and independent discovery of OH⁺ in two other PNe in the SPIRE spectra is also reported in this volume (see [Ettxaluze et al. 2014](#)). All five PNe (NGC 6445, NGC 6720, and NGC 6781 in HerPlaNS, as well as NGC 7293 and NGC 6853) are molecule rich, with ring-like or torus-like structures and hot central stars ($T_{\text{eff}} > 100\,000$ K). The OH⁺ emission is most likely due to excitation in a PDR. Although other factors such as high density and low C/O ratio may also play a role in the enhancement of the OH⁺ emission, the fact that we do not detect OH⁺ in objects with $T_{\text{eff}} < 100\,000$ K suggests that the hardness of the ionising central star spectra (i.e. the production of soft X-rays, $\sim 100\text{--}300$ eV) could be an important factor in the production of OH⁺ emission in PNe.

Acknowledgements. We thank the anonymous referee for the invaluable suggestions to improve this paper. Studies of interstellar chemistry at Leiden Observatory are supported through the advanced-ERC grant 246976 from the European Research Council, through a grant by the Dutch Science Agency, NWO, as part of the Dutch Astrochemistry Network, and through the Spinoza prize from the Dutch Science Agency, NWO. I.A. is thankful for useful discussions with F. S. Cambiazo, M. Kama, and R. Meijerink. Support for this work was provided by NASA through an award issued by JPL/Caltech in support of *Herschel* Guest Observer programs (Ueta, Ladjal, Kastner, Sahai), by the Japan Society of the Promotion of Science through a FY2013 long-term invitation fellowship program (Ueta). K.M.E. and P.v.H. acknowledges support from the Belgian Science Policy Office through the ESA/PRODEX program. R.Sz. and N.S. acknowledge support from the Polish NCN grant 2011/01/B/ST9/02031. J.H.K.'s and R.M.'s research on planetary nebulae is supported via award numbers GO3-14019A to RIT and GO3-14019B to Vanderbilt University (respectively) issued by the *Chandra* X-ray Observatory Center, which is operated by the Smithsonian Astrophysical Observatory for and on behalf of NASA under contract NAS803060. This work is based on observations made with the *Herschel* Space Observatory, a European Space Agency (ESA) Cornerstone Mission with significant participation by NASA.

References

- Aleman, I., & Gruenwald, R. 2011, *A&A*, 528, A74
 Bachiller, R., Forveille, T., Huggins, P. J., & Cox, P. 1997, *A&A*, 324, 1123
 Barlow, M. J., Swinyard, B. M., Owen, P. J., et al. 2013, *Science*, 342, 1343
 Barsuhn, J., & Walmsley, C. M. 1977, *A&A*, 54, 345
 Bekooy, J. P., Verhove, P., Meerts, W. L., & Dymanus, A. 1985, *J. Chem. Phys.*, 82, 3868
 Benítez, G., Vázquez, R., Zavala, S., et al. 2005, in *Planetary Nebulae as Astronomical Tools*, eds. R. Szczerba, G. Stasińska, & S. K. Gorny, AIP Conf. Ser., 804, 64
 Benz, A. O., Bruderer, S., van Dishoeck, E. F., Staeuber, P., & Wampfler, S. F. 2013, *J. Phys. Chem. A*, 117, 9840
 Cohen, M., & Barlow, M. J. 2005, *MNRAS*, 362, 1199
 de Almeida, A. A. 1990, *Rev. Mex. Astron. Astrofis.*, 21, 499
 Draine, B. T., & Bertoldi, F. 1996, *ApJ*, 468, 269
 Drouin, B. J. 2013, *J. Phys. Chem. A*, 117, 10076
 Ettxaluze, M., Cernicharo, J., Goicoechea, J. R., et al. 2014, *A&A*, 566, A78
 Gerin, M., de Luca, M., Black, J., et al. 2010, *A&A*, 518, L110
 González-Alfonso, E., Fischer, J., Bruderer, S., et al. 2013, *A&A*, 550, A25
 Griffin, M. J., Abergel, A., Abreu, A., et al. 2010, *A&A*, 518, L3
 Guerrero, M. A., Chu, Y.-H., Gruendl, R. A., Williams, R. M., & Kaler, J. B. 2001, *ApJ*, 553, L55
 Gupta, H., Rimmer, P., Pearson, J. C., et al. 2010, *A&A*, 521, L47
 Hasegawa, T. I. 2003, in *Planetary Nebulae: Their Evolution and Role in the Universe*, eds. S. Kwok, M. Dopita, & R. Sutherland, IAU Symp., 209, 249
 Henry, R. B. C., Kwitter, K. B., & Dufour, R. J. 1999, *ApJ*, 517, 782
 Herbst, E., & Klemperer, W. 1973, *ApJ*, 185, 505
 Hollenbach, D., Kaufman, M. J., Neufeld, D., Wolfire, M., & Goicoechea, J. R. 2012, *ApJ*, 754, 105
 Hora, J. L., Latter, W. B., & Deutsch, L. K. 1999, *ApJS*, 124, 195
 Huggins, P. J., Bachiller, R., Cox, P., & Forveille, T. 1996, *A&A*, 315, 284
 Indriolo, N., Neufeld, D. A., Gerin, M., et al. 2012, *ApJ*, 758, 83
 Kama, M., López-Sepulcre, A., Dominik, C., et al. 2013, *A&A*, 556, A57
 Kastner, J. H., Montez, Jr., R., Balick, B., et al. 2012, *AJ*, 144, 58
 Kastner, J. H., Weintraub, D. A., Gatley, I., Merrill, K. M., & Probst, R. G. 1996, *ApJ*, 462, 777
 Kimura, R. K., Gruenwald, R., & Aleman, I. 2012, *A&A*, 541, A112
 Kristensen, L. E., van Dishoeck, E. F., Benz, A. O., et al. 2013, *A&A*, 557, A23
 López-Sepulcre, A., Kama, M., Ceccarelli, C., et al. 2013, *A&A*, 549, A114
 Meijerink, R., & Spaans, M. 2005, *A&A*, 436, 397
 Meijerink, R., Spaans, M., Loenen, A. F., & van der Werf, P. P. 2011, *A&A*, 525, A119
 Müller, H. S. P., Schlöder, F., Stutzki, J., & Winnewisser, G. 2005, *J. Mol. Struct.*, 742, 215
 Neufeld, D. A., & Dalgarno, A. 1989, *ApJ*, 340, 869
 Neufeld, D. A., Goicoechea, J. R., Sonnentrucker, P., et al. 2010, *A&A*, 521, L10
 O'Dell, C. R., Balick, B., Hajian, A. R., Henney, W. J., & Burkert, A. 2002, *AJ*, 123, 3329
 O'Dell, C. R., Ferland, G. J., Henney, W. J., & Peimbert, M. 2013, *AJ*, 145, 92
 Pereira-Santaella, M., Spinoglio, L., Busquet, G., et al. 2013, *ApJ*, 768, 55
 Peterson, K. I., Fraser, G. T., & Klemperer, W. 1984, *Can. J. Phys.*, 62, 1502
 Phillips, J. P. 2003, *MNRAS*, 344, 501
 Phillips, J. P. 2006, *MNRAS*, 368, 819
 Phillips, J. P., Williams, P. G., Mampaso, A., & Ukita, N. 1992, *Ap&SS*, 188, 171
 Phillips, J. P., Ramos-Larios, G., & Guerrero, M. A. 2011, *MNRAS*, 415, 513
 Pickett, H. M., Poynter, R. L., Cohen, E. A., et al. 1998, *J. Quant. Spectr. Rad. Transf.*, 60, 883
 Pilbratt, G. L., Riedinger, J. R., Passvogel, T., et al. 2010, *A&A*, 518, L1
 Poglitsch, A., Waelkens, C., Geis, N., et al. 2010, *A&A*, 518, L2
 Pottasch, S. R., & Bernard-Salas, J. 2010, *A&A*, 517, A95
 Rangwala, N., Maloney, P. R., Glenn, J., et al. 2011, *ApJ*, 743, 94
 Sahai, R., Morris, M. R., & Villar, G. G. 2011, *AJ*, 141, 134
 Smith, N. 2003, *MNRAS*, 342, 383
 Sternberg, A., & Dalgarno, A. 1995, *ApJS*, 99, 565
 Tielens, A. G. G. M. 2005, *The Physics and Chemistry of the Interstellar Medium* (Cambridge University Press)
 Ueta, T., Ladjal, D., Exter, K. M., et al. 2014, *A&A*, 565, A36
 van der Tak, F. F. S., Nagy, Z., Ossenkopf, V., et al. 2013, *A&A*, 560, A95
 van der Werf, P. P., Isaak, K. G., Meijerink, R., et al. 2010, *A&A*, 518, L42
 van Dishoeck, E. F., Kristensen, L. E., Benz, A. O., et al. 2011, *PASP*, 123, 138
 Werner, H.-J., Rosmus, P., & Reinsch, E.-A. 1983, *J. Chem. Phys.*, 79, 905
 Wesson, R., Cernicharo, J., Barlow, M. J., et al. 2010, *A&A*, 518, L144
 Wyrowski, F., Menten, K. M., Güsten, R., & Belloche, A. 2010, *A&A*, 518, A26
 Zack, L. N., & Ziurys, L. M. 2013, *ApJ*, 765, 112
 Zijlstra, A. A., Chapman, J. M., te Lintel Hekkert, P., et al. 2001, *MNRAS*, 322, 280
 Zuckerman, B., Kastner, J. H., Balick, B., & Gatley, I. 1990, *ApJ*, 356, L59